

## Article

# Research into Dynamic Error Optimization Method of Impeller Blade Machining Based on Digital–Twin Technology

Rongyi Li <sup>1,\*</sup>, Shanchao Wang <sup>1</sup>, Chao Wang <sup>2</sup>, Shanshan Wang <sup>2</sup>, Bo Zhou <sup>2</sup>, Xianli Liu <sup>1</sup> and Xudong Zhao <sup>1</sup><sup>1</sup> School of Mechanical Power Engineering, Harbin University of Science and Technology, Harbin 150080, China<sup>2</sup> China Aerospace Science and Technology Corporation No. 8 Academy–Shanghai Institute of Spacecraft Equipment, Shanghai 200000, China

\* Correspondence: easy198766@126.com

**Abstract:** A TC4 impeller blade is a typical weak, rigid, thin-walled part. The contact area between a cutting tool and a workpiece has strong time-varying characteristics. This leads to a strong non-linear variation in cutting load. So, in this kind of part, the processing error is difficult to control. To solve this problem, a method of processing error prediction and intelligent controlling which considers the effect of tool wear time variation is proposed by combining digital-twinning technology. Firstly, an iterative model for digital-twin process optimization is constructed. Secondly, an iterative prediction model of the machining position following the milling force and considering the effect of tool wear is proposed. Based on these models, the machining error of the TC4 impeller blade under dynamic load is predicted. Dynamic machining error prediction and intelligent control are realized by combining the digital-twin model and the multi-objective process algorithm. Finally, the machining error optimization effect of the proposed digital-twin model is verified via a comparison experiment of impeller blade milling. In terms of the precision of milling force mapping, the average error after optimization is less than 8%. The maximum error is no more than 14%. In terms of the optimization effect, the average error of the optimized workpiece contour is reduced by about 20%. The peak contour error is reduced by approximately 35%.

**Keywords:** digital-twin; impeller blade processing; optimization of machining errors; milling force



**Citation:** Li, R.; Wang, S.; Wang, C.; Wang, S.; Zhou, B.; Liu, X.; Zhao, X. Research into Dynamic Error Optimization Method of Impeller Blade Machining Based on Digital–Twin Technology. *Machines* **2023**, *11*, 697. <https://doi.org/10.3390/machines11070697>

Academic Editor: Yuwen Sun

Received: 28 April 2023

Revised: 14 June 2023

Accepted: 19 June 2023

Published: 1 July 2023



**Copyright:** © 2023 by the authors. Licensee MDPI, Basel, Switzerland. This article is an open access article distributed under the terms and conditions of the Creative Commons Attribution (CC BY) license (<https://creativecommons.org/licenses/by/4.0/>).

## 1. Introduction

The digital-twin concept was inspired by the in-orbit and assembly technology utilized by NASA in the Apollo mission in 1969. By creating “twins” of on-orbit products, a digital-twin can reflect (or mirror) the state of the spacecraft carrying out missions [1]. In 2005, Professor Michael Greaves from the University of Michigan introduced the idea of “the Mirrored Spaces Model (MSM)” [2]. Tao Fei et al. [3,4] proposed six application principles for digital-twins based on the five-dimensional structure model of a digital-twin. They explored the key issues and technologies that need to be addressed during the design and implementation of 14 types of applications driven by digital-twins. Liu, Jinfeng et al. [5] proposed a method for constructing a digital-twin process model (DTPM) based on knowledge-evolution machining features. The method solves three key technologies: the associated structure of process knowledge, the expression method of evolutionary geometric features, and the association mechanism between them.

In terms of digital-twin applications in manufacturing processes, Albrecht Hänel et al. [6] utilized a fundamental digital-twin structure to investigate the creation of digital-twins for manufacturing processes. Bao, Jinsong. et al. [7] extended and integrated models of cutting force and tool engagement to construct a complete digital-twin model of cutting load. In this model, the interactive operation model of the digital-twin is used for interaction between the physical space and the virtual space. Delbrugger, T. et al. [8] proposed a new concept of systematically simulating the variability in the production system in the

digital-twin of the production entity. This concept is an essential stepping stone for the more powerful simulation-based optimization of the production system. Although scholars have had slightly different points of concern in defining a digital-twin, there are two consensuses: each definition emphasizes the connection between the physical model and the corresponding virtual model or virtual copy, and the connection is established using sensors to generate real-time data. Luo, Weichao. et al. [9] researched digital-twins for CNC machine tools, establishing a multi-domain unified modeling method for DT, exploring the mapping strategy between physical and digital spaces, and proposing autonomous DT strategies. Sun Xuemin. et al. [10] presented a digital-twin-driven assembly and debugging method for the complex assembly process of high-precision products, successfully applying it to the assembly process of aerospace-type high-precision servo valves. Albrecht Hänel et al. [11] presented a method for creating a digital-twin model based on process planning and process data by incorporating the attributes and relationships of relevant information and data involved in the manufacturing process. Liu, Shimin et al. [12] proposed a digital-twin modeling method based on bionics principles for the processing of aerospace parts, developing multiple digital-twin sub-models through this method. These sub-models interact with each other and constitute the expression of the complete real process. T. Mukherjee et al. [13] showed that using digital-twins in 3D printing can reduce the amount of trial-and-error testing, reduce defects, and shorten the time between design and production. R. Söderberg et al. [14] demonstrated that the real-time control and optimization of digital-twins in production systems is helpful in achieving personalized production. Glatt, M. et al. [15] proposed an integrated system based on physical simulations for small-batch manufacturing, consisting of a material processing system and its digital-twin.

Digital-twin technology has made certain progress in optimizing the processing process. Further research is needed on the applicability of digital-twin models to specific processing needs. In addition, the lack of effective evaluation methods for processing technology indicators and knowledge bases greatly hinders the further development of digital-twin technology.

The formation, prediction, and compensation of machining errors have been studied extensively. Machining error prediction and compensation caused by milling force is one of the main directions in this field. Lili Zhao et al. [16] proposed a dynamic optimization method of cutting parameters based on the simulation optimization of virtual twins and the dynamic perception of physical machining conditions. Ratchev et al. [17] utilized a theoretical flexible force-deflection model to predict and compensate for machining error by optimizing the tool path prior to commencing machining operations. Similarly, Weifang Chen et al. [18] proposed a dynamic model to predict the deformation of thin-walled parts during multi-layer machining by taking into account the coupling relationship between cutting force and machining deformation. This method incorporates the concept of multi-layer compensation. Wang, Liping et al. [19] proposed a cutting workpiece engagement (CWE) extraction method to calculate milling force and identify machining geometric changes during milling. An iterative method for machining deformation calculation was established by considering the coupling effect of milling force and tool workpiece deformation. Liu, Changqing et al. [20] employed a dynamometer to obtain milling force data and utilized the obtained dynamic characteristics to solve the error. They also proposed a real-time machining error compensation strategy. Yue, Caixu [21] proposed a method to calculate milling force based on time-varying chip thickness and coupled this force with the elastic deformation of the workpiece to predict surface error. Chen, Zhitao et al. [22] established a prediction model for the instantaneous uncut chip thickness of milling force by combining the theory of elastic deformation of thin-walled workpieces and the cutting area. An iterative calculation method was used to obtain the deformation matrix of the workpiece. The surface formation mechanism and workpiece deformation matrix were used to predict the machining error of thin-walled workpieces. Lastly, Ge et al. [23] proposed a rapid prediction method for cutting-force-induced errors in thin-walled parts. This method

considered the dynamic interaction between the tool and the workpiece based on the global stiffness matrix. These methods can significantly improve the precision and quality of machining operations. Sun, Yuwen et al. [24–26] discretized thin-walled parts and tools into differential elements. A precise modeling method for dynamic milling systems considering both force-induced deformation and multi-point contact structural dynamics in the contact zone was proposed. The extended second-order semi discretization method was used to predict the flutter stability of the system.

The errors caused by milling force in the machining process of thin-walled parts were deeply studied by the above scholars, and strategies such as multi-layer compensation and real-time compensation were proposed. However, when solving the milling force leading to elastic deformation, the main methods used at present are mainly to integrate the instantaneous cutting thickness and to solve it via CWE. Due to the current research on solving the milling force, these two kinds of methods are the approximate expression of the cutting relationship. There are precision problems in solving the milling force, which also affects the subsequent strategy. The calculation process of this method is complicated, and the feedback time is long. So, it is difficult to meet the requirements of digital-twin models for processing optimization feedback.

In this paper, a digital-twin model of the machining process of impeller blades is established. The model uses the finite element method to accurately calculate the chip contact area considering the impact of tool wear. This model can more accurately predict dynamic milling forces. This article analyzes the complex coupling relationship between milling force and machining error by establishing a predictive model for the variation in machining error with machining position. Finally, this article combines digital-twin technology with a genetic algorithm to achieve the iterative optimization of machining process errors.

## 2. Digital-Twin Model Based on Specific Processing Technology

### 2.1. Digital-Twin Optimization Model Based on Specific Processing Technology

This study applies a digital-twin model to a specific process as the research object, and the model's composition and operation process is showcased in Figure 1 below.

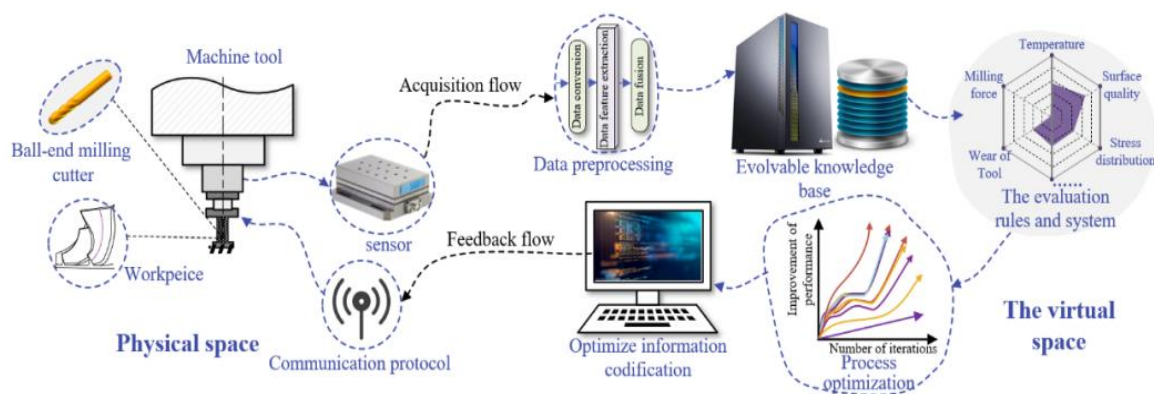


**Figure 1.** Digital-twin model for specific processing procedures.

As shown in Figure 1, the process optimization model is mainly composed of physical space and virtual space. The left part of the figure is the physical space. It is composed of a five-axis machining machine tool, a Daijie double-edge integral carbide ball-end milling cutter, a Kistler9257B dynamometer (Kistler, Winterthur, Switzerland), sensors (acceleration sensor, acoustic emission sensor, etc.), and workpiece materials. The function of physical space provides the actual machining information of the workpiece material for the iterative mechanism of the digital-twinning system. The blue and black dashed arrows illustrate the flow of data within and between physical and virtual spaces, respectively. In the virtual space, the collected data undergoes a series of transformations. The digital-twin

system includes a data preprocessing module, an evolutionary knowledge base module, an evaluation rule and evaluation system module, a process optimization module, and an optimization information encoding module before returning to the physical space. This cycle represents an iteration of the digital–twin model, enabling the ongoing optimization of the impeller blade machining process. The six modules comprising the virtual space depicted in Figure 1 are crucial components of the digital–twin model, with particular emphasis on the evolvable knowledge base module. The following article will introduce the contents and operation rules of each module in detail, as shown in Figure 2.

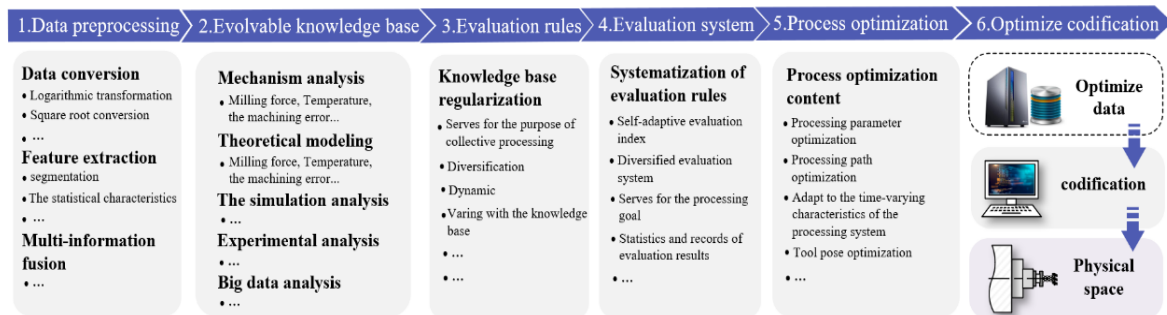


**Figure 2.** The components of the virtual space of the digital–twin model.

The digital–twin model described in this paper comprises six modules that work in concert to optimize the impeller blade machining process. These modules are:

(1) Data preprocessing module

This includes data conversion, feature extraction, and multiple information fusion components. The module extracts and collects machining signals such as cutting force information, machine tool spindle spatial position information, and the angle of the rotary table. This module transmits and prestores data. After data conversion, feature extraction, and multi–information fusion, the first sorting and classification steps are carried out. Secondly, the information is stored for the multi–layer optimization of data processing. This module sequentially performs data denoising, removes redundancy, and supplements missing values on the pre stored data. The processed data are transmitted to the evolvable knowledge base module.

(2) Evolvable knowledge base module

This passes the processed data information flow into the acceptance layer of the evolvable knowledge base module. Information is initially stored in the acceptance layer and then passed to the knowledge base storage layer. Then, the tool wear rule model and the tool milling force model are established in the model layer. The knowledge base storage layer contains the physical acquisition data and virtual operation data that facilitate the physical–virtual space interaction. The module adapts to the feedback of actual machining conditions. With each iteration, the mapping of physical space will become more and more accurate.

(3) Process evaluation rule module

The information collected in the evolvable knowledge base is analyzed based on the modeling results. The evolvable rules are defined according to the modeling results.

(4) The process evaluation system module

This provides an overall evaluation of the process based on data output from the process.

(5) The process optimization module

This optimizes processing parameters, processing paths, processing tools, and other aspects using the overall process evaluation results as input.

(6) Optimize the information digitization module

This transmits the real-time angle of a five-axis machine tool rotation table, impeller profile information, the real-time position of the cutting tool, spindle speed, and other processing information to the virtual space by using the API8070 communication mode. The digital-twin model provides an implementation scheme for optimizing the specific processing level. The digital-twin model based on TC4 impeller blade processing technology is established in this paper, and the model will be used to optimize the process in the following chapters.

## 2.2. TC4 Impeller Blade Machining Digital-Twin Model

In this chapter, the digital-twin model for impeller blade processing will be introduced. The digital-twin model is in the form of Professor Tao Fei's [3] five-dimensional model. The model comprises a physical entity, a virtual entity, twin data, a service, and connection. In terms of structure, the virtual space includes a virtual entity, twin data, a service, and other components. The evolvable knowledge base module in the virtual space contains the virtual entity and twin data. The five-dimensional model is used to show the flow relationship between the data modules, as depicted in Figure 3.

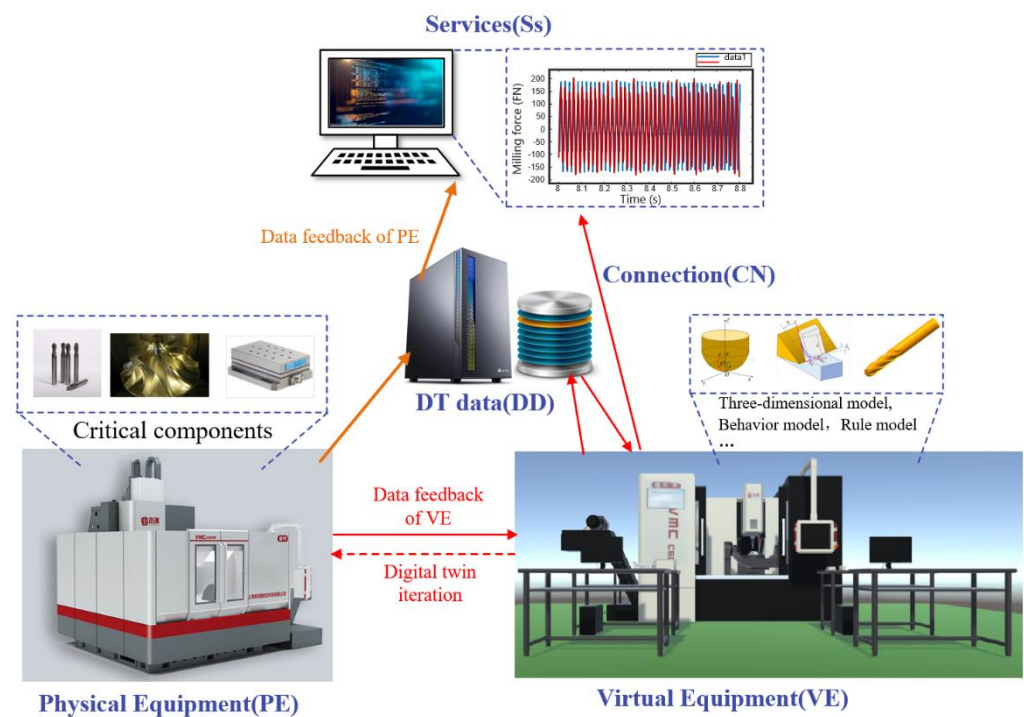


**Figure 3.** Digital-twin model of impeller blade processing.

This paper establishes a digital-twin model of a machine tool and workpiece, which includes a subsystem and a deployed sensor. The machine is an open five-axis vertical CNC milling center. An experimental Kistler9257B dynamometer and Kistler5007 (Kistler, Winterthur, Switzerland) charge amplifier were used to collect cutting force signals. The sampling frequency of the data is 8000 Hz. The evolvable knowledge base module utilizes a 3D model of machine tools, workpieces, tools, and other physical entities. This study takes inputs such as the spatial position information of the machine tool spindle and the angle of the rotary table to predict and evaluate dynamic milling forces and dynamic machining errors based on sensor data. The digital-twin model consists of three data streams: physical entity data feedback, virtual entity data feedback, and the iteration of the digital-twin model. Physical entity data feedback involves the process of reading information from sensors and transmitting it to the service section for visualization. Virtual entity data feedback involves transmitting machine position and pose information to the virtual entity in the virtual space. The virtual entity updates the twin data and returns it to

itself, providing real-time feedback to the physical entity that affects the actual machining process. The services section visualizes these data. The iteration of the digital-twin model occurs after the completion of the working procedure, where the virtual space optimizes the working procedure based on feedback information obtained from the process and feeds it back to the machine tool.

### 3. Digital-Twin Model Evolvable Knowledge Base Module

#### 3.1. Solution of Tool-Workpiece Cutting Contact Relationship

The calculation of milling force is mainly based on the integral of undeformed chip thickness or cutting contact area. The effect of tool wear is often ignored when solving the cutting contact relationship between tool and workpiece. These characteristics limit the effectiveness in digital-twin systems. To solve these problems, the finite element software ABAQUS is used to simulate the milling process. In this method, ABAQUS secondary development was used to carry out the simulation calculation. The system sets the spindle speed, cutting depth, and feed rate as the main parameters of the machining process. Under different parameter conditions, the extraction of tool workpiece contact stress point clouds can be achieved to determine effective cutting participation points.

The interaction between the cutting tool and the workpiece involves complex position and attitude changes. In order to simplify the machining process, square thin-walled parts can be used to replace the machining of impeller blades. The simulation of machining parameters and the machining positions of thin square plates are derived from 128 groups of typical machining situations in the machining process of impeller blades. Among them, the finite element simulation results of extracting the position and pose information of a certain cutting tool are shown in Figure 4.

In Figure 4,  $\theta$  and  $\lambda$  denote the rake and side rake angle, respectively, of the tool under a specific set of processing parameters. The red schematic points represent stress responses obtained from finite element simulations, which provide accurate solutions for the contact area of the chip. The curves in the four groups of simulated tool paths depict the total contact area of the tool and chip output via the finite element model, which are subject to some degree of inaccuracy due to factors such as contact condition settings, mesh size selection, and hardware limitations of the simulation computer. These limitations may lead to some level of data imprecision. The 128 sets of analysis results generated by the simulations are stored in the data storage component of the evolvable knowledge base module.

In the practical machining of impeller blades, the digital-twin model can continuously receive real-time machining parameters and pose information via the machine tool's communication protocol. Directly feeding these data into the finite element model to calculate the tool-chip contact area would significantly slow down the operation and feedback of the digital-twin model. To expedite the solution of the tool-chip contact area, the read information can be compared and interpolated with the data storage component of the evolvable knowledge base module. A higher quantity of information stored in the evolvable knowledge base would lead to a more precise determination of the tool-chip contact area.

#### 3.2. Revised Model of Unreformed Cutting Thickness under Tool Wear Conditions

During the ball-end milling cutter section of the cutting process, the cutting edge experiences both rotary motion of the tool and translation movement along the feed direction. A double-bending chip is generated at the apex of the ball-end milling cutter along the cutter helix. This chip-bending phenomenon is closely related to the tool-workpiece cutting contact conditions. The instantaneous undeformed cutting thickness of the ball-end milling cutter is strongly associated with the geometric parameters of the cutter.

As shown in Figure 5, the instantaneous uncut chip thickness in ball-end milling under the condition of no tool wear [27] is as follows:

$$h(\psi_{ji}, z_i) = f_z \sin \psi_{ji} \sin \kappa \quad (1)$$

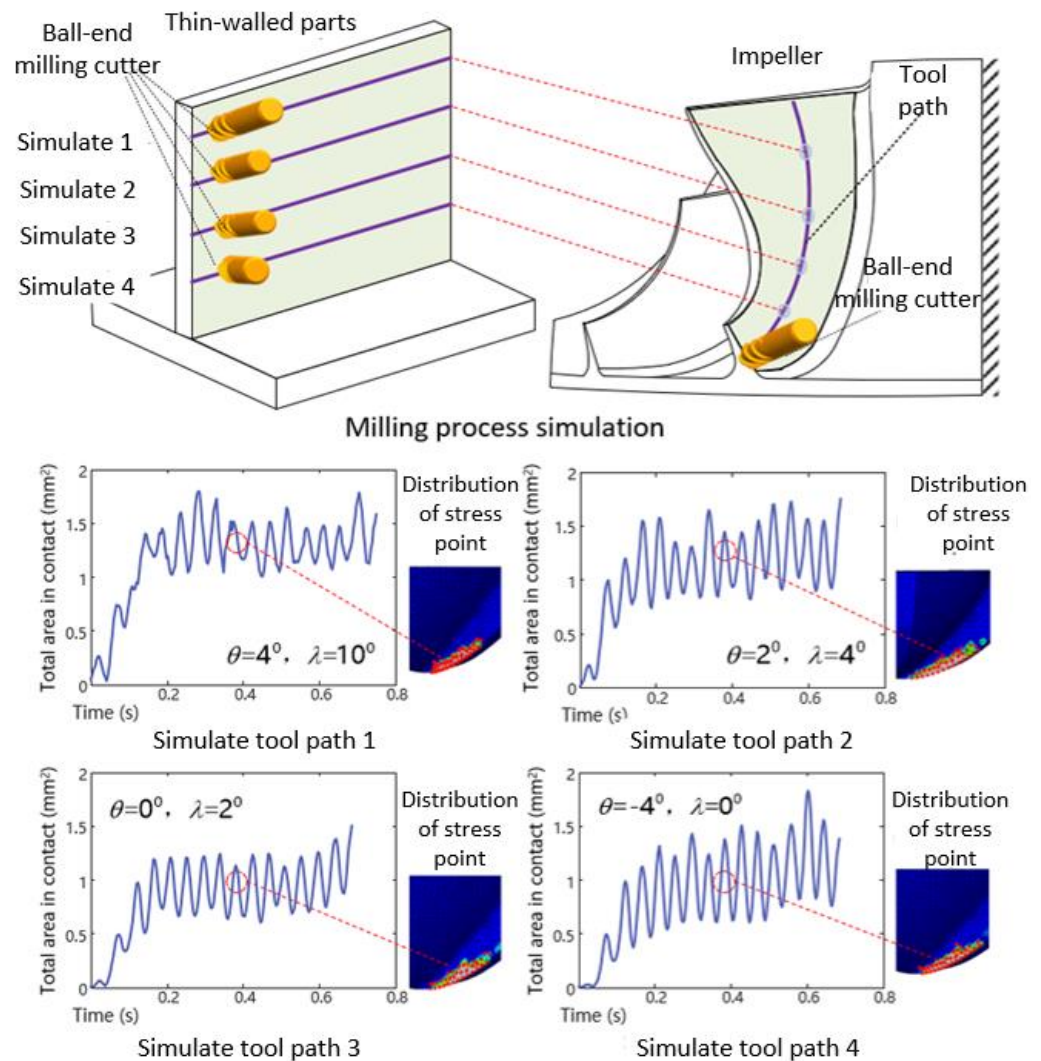


**Figure 4.** Milling simulation and tool–chip contact area solution.

In the formula,  $f_z$  represents the cutter's feed per tooth (mm/z);  $\psi_{ji}$  is the instantaneous radial cutting contact angle (rad) at the spatial position of the  $i$ -th cutting element on the  $j$ -th cutter tooth;  $\kappa$  is the axial immersion angle (rad) of the tool and the workpiece.

### 3.2.1. Construction of an Evolutionary Knowledge Base Model Based on Tool Wear Prediction Model

Through the use of machine tool communication protocols, the evolutionary knowledge base is capable of reading machining parameters and posture data in real time from the cutting tool, as well as gathering and storing information about the tool's pose. To expedite the resolution of tool–chip contact areas during the cutting process, the information obtained from the machine tool is compared and extrapolated with the data stored in the evolutionary knowledge base module. In the virtual environment, a model of the unreformed cutting thickness under the condition of tool wear and a model of the tool milling effort in the presence of wear are constructed first. The evolutionary knowledge base is utilized to solve the dynamic cutting force based on rolling data, which is then transmitted to the process evaluation rule module. The resulting process's overall evaluation data

are then relayed to the process optimization module, where the optimization of process parameters is performed.

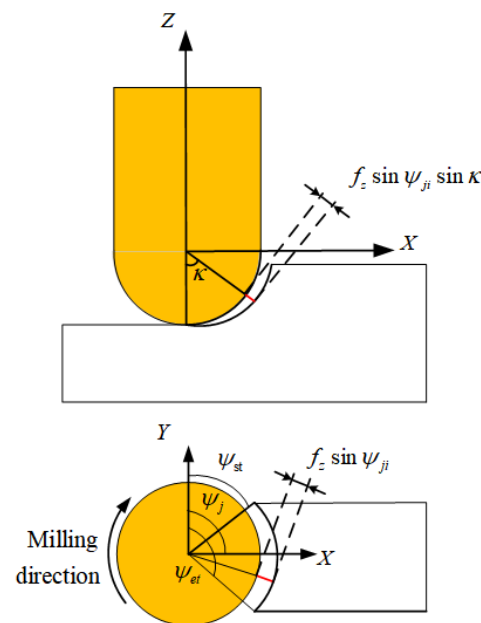


**Figure 5.** Instantaneous undeformed cutting thickness in ball-end milling.

To establish an evolvable knowledge base, the first step is to establish tool wear rules. The cutting force and the hardness of the workpiece and tool can cause friction extrusion, adhesion, diffusion, edge collapse, and plastic deformation, which lead to tool wear and damage. When a tool is worn to a certain extent, it will affect the processing quality and efficiency. A comprehensive analysis of the micro-section of the tool is carried out by cutting the tool section in the  $XY$  plane and cutting the surface at the micro-level to approximate it as a turning tool. The force on the selected point is analyzed by taking five evenly spaced points in the intercepting plane for solution. In this article, point 4 is selected as a case for analysis. The cutting force at point 4 can be divided into three parts: the tangential component  $dF_t$  along the cutting edge, the radial component  $dF_r$  perpendicular to the tool center axis, and the axial component  $dF_a$  along the tool axis. The direction of  $dF_a$  is along the  $Z$ -axis and is not considered in the  $XY$  plane, as shown in Figure 6.

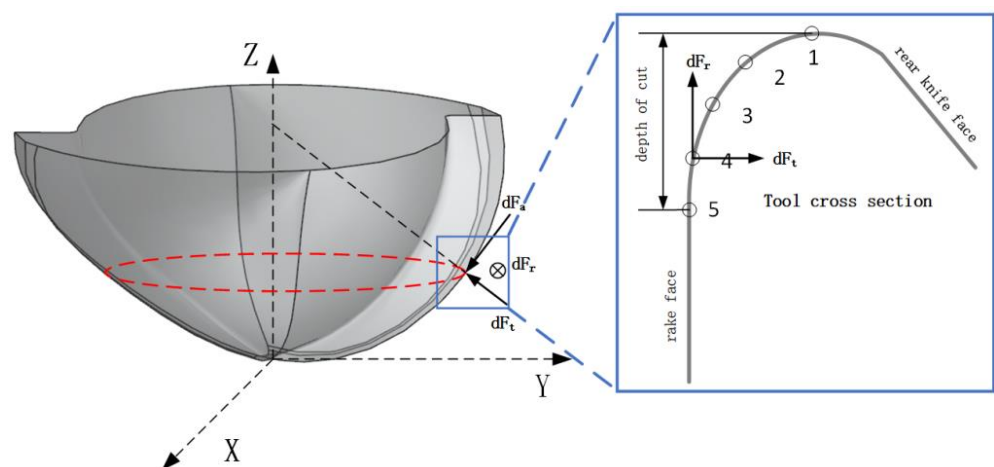


**Figure 6.** Microscopic force analysis at point 4.

### 3.2.2. Analysis

Tool metals consist of polycrystalline structures composed of numerous grains of varying shapes. These grains undergo plastic deformation that leads to changes in the lattice arrangement within the metal. The presence of external forces induces shear stress in the material, which causes the lattice to undergo elastic deformation when the stress is small. However, as the stress exceeds a certain threshold, the resistance of the lattice is overcome, causing the grains to slide relative to one another along a crystal plane, a phenomenon referred to as slip. After a certain displacement, the atoms stabilize in a new position, and the slip along the plane ceases due to an increase in resistance. The continued application of shear stress leads to the propagation of slip in other facets of the crystal, resulting in plastic deformation and eventual tool wear.

The formula of the tool wear rule [28,29] is as follows:

$$V = kSF_nH^{-1} \quad (2)$$

In the formula,  $V$  is the wear amount ( $\text{mm}^3$ ) and  $k$  is the empirical wear coefficient ( $\text{m}^{-1}\text{N}^{-1}$ ).  $S$  is the sliding distance (m),  $F_n$  is the normal force (N), and  $H$  is the Vickers hardness number of harder materials.

Where  $k$  is the empirical wear coefficient, the calculation formula [30] is

$$k = vSF_n \quad (3)$$

In the formula,  $v$  is the cutting speed (m/min),  $S$  is the sliding distance (m), and  $F_n$  is the normal force (N).

According to the model of tool volume wear, the influence of three stages of tool wear on tool wear was comprehensively considered. The iterative change in the cross-section boundary at point 4 is shown in Figure 7.

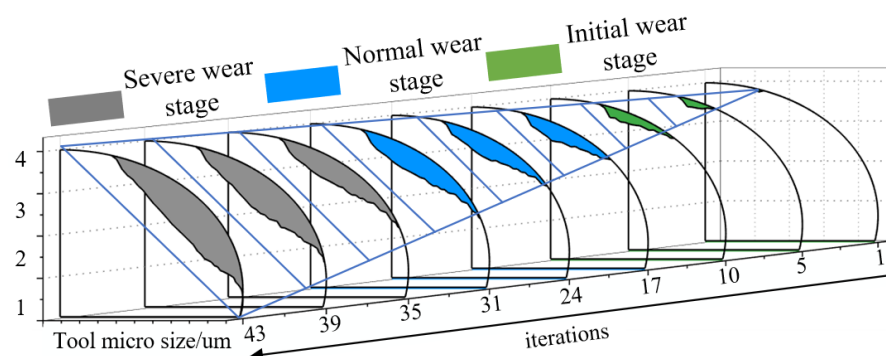


**Figure 7.** Point 4 wear boundary process diagram.

As shown in Figure 7, point 4 was selected for wear iteration. The different colors in the figure represent different stages of wear and tear. Green represents the initial wear stage of the tool, blue represents the normal wear stage, and gray represents the sharp wear stage. At the bottom right of the picture is the number of iterations. The direction of the arrow in the picture is the increase in the number of iterations. The number corresponds to the change in the tool wear boundary at the selected point 4. The cutting analysis was carried out for other selected points, and the wear boundary in Figure 8 was obtained after superimposed wear.

As shown in Figure 8, the figure shows the number of iterations on the right, divided into 5, 24, and 43 iterations. The 5 iterations correspond to the initial tool wear stage, the 24 iterations are the normal wear stage, and the 39 iterations are the severe wear stage. Each row corresponding to the number of iterations is the wear boundary of each selected point; the first four graphs of each column are the wear boundaries of points 5, 4, 3, and 2, and the fifth graph is the integrated boundary of the first four points. The first four columns are

the changes in the wear boundary for each selected point. The fifth column is the boundary iteration change curve of the overall tool. Considering the influence of the three stages of tool wear on tool wear, the overall change curve of tool section wear is shown in Figure 8.

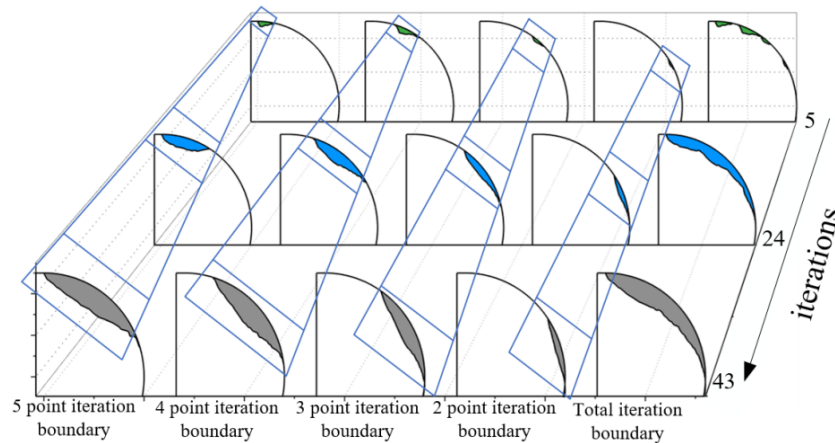


Figure 8. Microscopic diagram of tool cross-section wear process.

As shown in Figure 9, different colors represent different stages of wear. Green is the early wear stage of the tool, blue is the normal wear stage, and gray is the rapid wear stage. The lower right of the figure is the number of iterations, and the direction of the arrow is the increase in the number of tool iterations. Each iteration number corresponds to the overall tool boundary of that iteration. Along with the direction of the arrow is the iterative change in the tool boundary. The tool used is a Dai-Jie double-blade integral carbide ball-end milling cutter, with a diameter of 10 mm, and the material is a hard alloy, as shown Table 1.

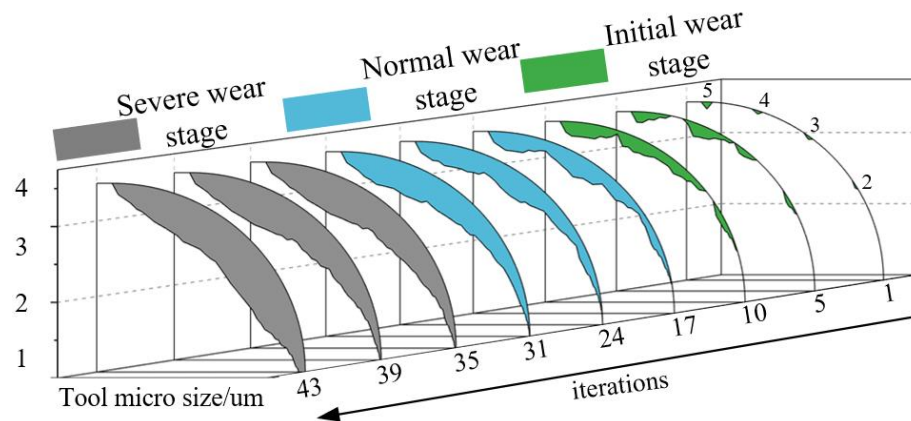


Figure 9. Variation trend of tool microscopic section boundary wear.

Table 1. Dai-Jie double-blade integral carbide material properties.

Parameter	Numerical Value	Parameter	Numerical Value
Density (kg/m <sup>3</sup> )	14,500	Hardness/HA	1154
Elasticity modulus/GPa	640	Heatconductivity coefficient (W/m·K)	75.4
Yield strength/MPa	2600	Poisson's ratio	0.22
Side rake angle/°	4	Helix angle/°	30
Number of cutting edges	2	Rake angle/°	2

The cutting depth of the tool is 0.2 mm, the rotating speed is 9200 r/min, and the speed  $v$  is

$$v = 2\pi Rn \tag{4}$$

When the tool rotates once during cutting, the blade only touches the workpiece at  $180^\circ$ , so the sliding distance  $S$  is

$$S = vt/2 \quad (5)$$

In the formula,  $t$  (min) is the contact time.

According to the calculation, the volume wear rate is about  $0.0003 \text{ mm}^3/\text{min}$ . A microscopic picture of tool wear is shown in Figure 10.

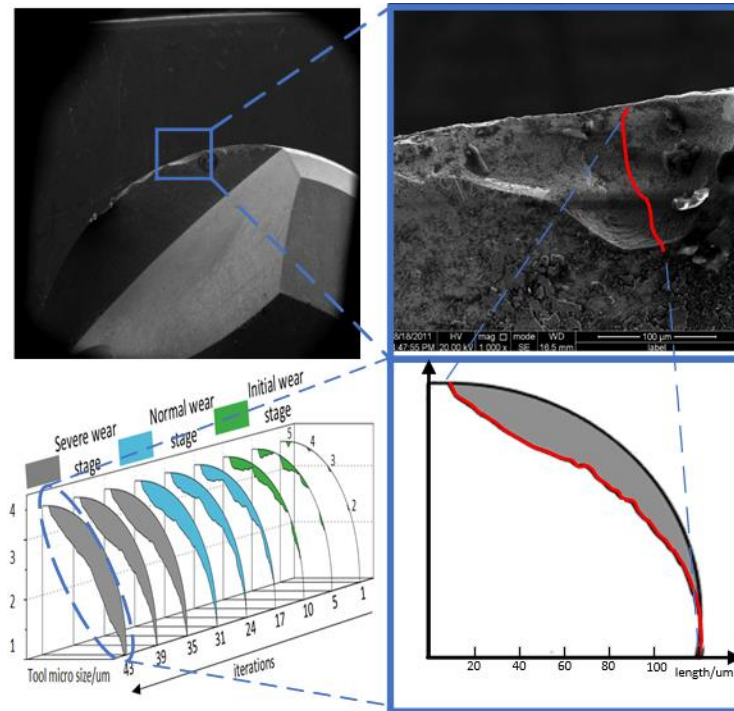


**Figure 10.** Comparison micrograph of tool wear.

In Figure 10, the upper half of the figure is the predicted tool wear boundary. The lower part of the figure is the tool wear boundary obtained from the experiment. The red curved boundary is the result of the experimental tool wear boundary and the predicted boundary of the 43rd iteration. There is a certain deviation between the two when compared. The reason for this is that in the method mentioned in this article, the wear volume  $V$  is a two-dimensional projection superposed on a certain section of the tool. This method can generate a three-dimensional volume of tool wear by stacking the changes in multi-layer two-dimensional projection, so as to achieve the accurate prediction of tool wear. The model can achieve optimal matching of prediction accuracy and efficiency by adjusting the number of contact points selected on the cross-section. Based on the above research, an evolutionary knowledge base model of the digital-twin tool wear prediction model is established.

During the cutting process, the tool wear causes the tool's volume to decrease, leading to changes in the axial immersion angle  $\kappa$  of the tool, as illustrated in Figure 11. The white part of the tool in the figure represents the worn volume of the tool. The reduction in tool volume is evident from the decrease in the axial immersion angle  $\kappa$ .

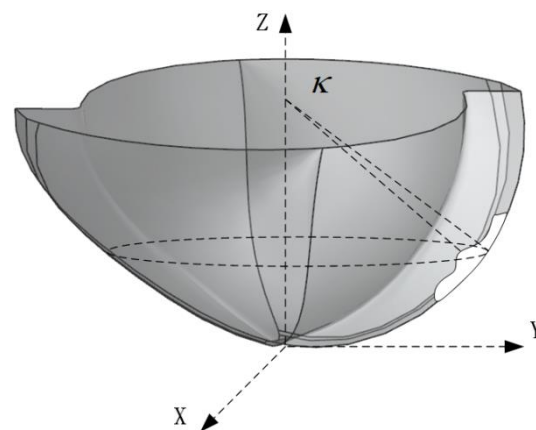


**Figure 11.** Variation trend of axial immersion angle.

From Figure 11, it is shown that the axial immersion angle  $\kappa$  will decrease with the tool wear, and the change formula of the axial immersion angle  $\kappa$  is

$$\kappa = \arctan \frac{\sqrt{2Ra_p - a_p^2}}{R - a_p} \quad (6)$$

In the formula,  $R$  is the radius.  $a_p$  is cutting depth.

The change formula of axial immersion angle  $\kappa$  was substituted into the formula of undeformed cutting thickness under the wear condition as follows:

$$h(\psi_{ji}, z_i) = f_z \sin \psi_{ji} \sin \arctan \frac{\sqrt{2Ra_p - a_p^2}}{R - a_p} \quad (7)$$

### 3.3. Milling Force Prediction Model Based on Tool–Chip Contact Relationship

The friction force on the tool flank face is related to the positive pressure and the wear of the flank face. The milling forces solved in this paper include those on the rake face and cutting edge. The partial force of the cutting edge is solved via the micro–element method, and the partial force of the rake face is solved by constructing the stress distribution of the rake face using the tool–chip contact relationship.

When calculating the partial forces on the cutting edge, the cutting edge is micro–elemented, and the force of each cutting edge element is related to the arc length of the element [31]. The calculation formula is as follows:

$$\begin{aligned} dF_{r1} &= K_{te} ds \\ dF_{t1} &= K_{re} ds \\ dF_{a1} &= K_{ae} ds \end{aligned} \quad (8)$$

In the formula,  $dF_{r1}$ ,  $dF_{t1}$ , and  $dF_{a1}$  are, respectively, the tangential force, radial force, and axial force components of the cutting edge element;  $ds$  is the arc length of the cutting edge element. By integrating the micro–element forces of the cutting edge, the  $dF_{r1}$ ,  $dF_{t1}$  and  $dF_{a1}$  components of the milling force received by the cutting edge can be obtained.  $K_{te}$ ,  $K_{re}$ ,  $K_{ae}$  use the milling force coefficient value calculated from the average milling force obtained through experiments proposed by GRADISEK [32].

When solving the component forces of the front cutter face, the solution model is the tool–chip contact mechanical model [33]. The specific situation of the model is shown in Figure 12.

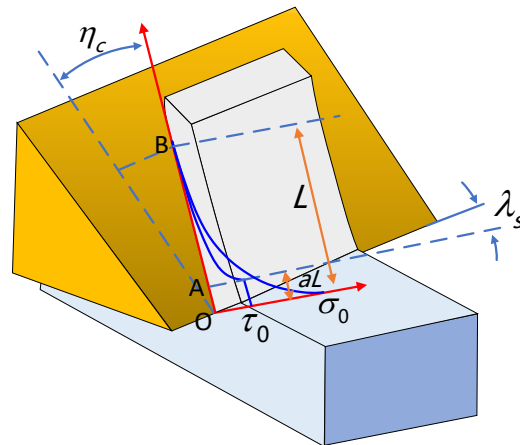


**Figure 12.** The tool–chip contact mechanics model.

In Figure 12,  $O$  is the tool tip,  $OA$  is the bonding area,  $AB$  is the sliding area, the maximum normal stress at the tool tip is  $\sigma_0$ , the tool–chip contact length is  $L$ , and the ratio of the bonding zone length to the tool–chip contact length is  $a$ . The friction stress  $\tau$  in the bonding area  $OA$  is a constant  $\tau_0$ , and the friction stress in the sliding area is the product of the normal stress and the friction factor. The normal stress  $\sigma$  conforms to the power exponential distribution:

$$\sigma(x) = \sigma_0 \left( \frac{L-x}{L} \right)^b \quad (9)$$

$b$  is the power exponent, and related experimental studies have shown that the value of  $b$  is around 3 [34]. The maximum stress at the tool tip can be solved using the friction stress  $\tau_0$  in the bonding area:

$$\sigma_0 = \tau_0 \frac{h}{L} \frac{\cos \eta_s \cos \beta_n}{\sin \phi_n \cos \eta_c \cos(\phi_n + \beta_n - \gamma_n)} \quad (10)$$

In the formula,  $h$  is the undeformed chip thickness,  $\eta_c$  is the cutting outflow angle,  $\eta_s$  is the shear outflow angle,  $\gamma_n$  is the normal angle of the rake face,  $\phi_n$  is the shear angle in the normal plane,  $\beta_n$  is the normal friction angle, and the size of  $\tau_0$  is close to the shear limit. At this time, the law of friction stress distribution is

$$\tau(x) = \begin{cases} \tau_0 & \tau(x) > \tau_0 \\ u\sigma(x) & \tau(x) < \tau_0 \end{cases} \quad (11)$$

In the formula,  $u$  is the sliding friction factor, and the size can be calculated from the ball mill test data or through an empirical formula. The scale factor  $a$  of the bond zone length to the tool–chip contact length can be solved using the empirical formula:

$$a = 1 - \left( \frac{\tau_0}{\sigma_0 u} \right)^{1/b} \quad (12)$$

The integral of normal stress on the rake face is equal to the positive pressure on the rake face, and the integral of friction stress on the rake face is equal to the friction force of the rake face.

$$F_\sigma = \int_0^L \sigma_0 (L-x)^b dx \quad (13)$$

$$F_f = \tau_0 a L + \int_{aL}^L u \sigma_0 \left( \frac{L-x}{L} \right)^b dx \quad (14)$$

In the formula,  $F_\sigma$  is the positive pressure on the rake face, and  $F_f$  is the friction force on the rake face.

The research object of the tool–chip contact mechanics model for stress distribution and milling force calculation is turning. The milling tool for impeller blade processing is a ball–end milling cutter, and the cutting method is different from turning. When using this model to solve the milling process, the model needs to be revised according to the milling situation. In the solution process, the stress response area is divided into  $N$  layers according to parameters such as depth of cut, tool inclination angle, and mesh size. The normal stress and friction force of each layer are as follows:

$$F_{\sigma g2k} = \frac{1}{N} \int_0^{L_k} \sigma_{0k} (L_k - x)^b dx \tag{15}$$

$$F_{fg2k} = \frac{1}{N} \left( \tau_0 a_k L_k + \int_{a_k L_k}^{L_k} u_k \sigma_{0k} \left( \frac{L_k - x}{L_k} \right)^b dx \right) \tag{16}$$

In the formula,  $F_{\sigma g2k}$  and  $F_{fg2k}$  are the normal stress and friction force of the rake face of the  $k$ -th ( $k = 1, 2, \dots, N$ ) layer, respectively;  $L_k$  is the tool–chip contact length extracted from the simulation results of the  $k$ -th layer;  $\sigma_{0k}$  is the maximum normal stress at the cutting edge of the  $k$ -th layer;  $a_k$  is the ratio of the  $k$ -th layer bonding area to the chip contact area; and  $N$  is the number of division layers.  $L_k$ ,  $\sigma_{0k}$ ,  $a_k$ , and other parameters can all be calculated from the tool–chip contact relationship obtained in 4–1.

The direction of the normal stress on the rake face  $F_{\sigma g2k}$  is perpendicular to the rake facing inward, and the direction of the friction force of  $F_{fg2k}$  is perpendicular to the normal stress and opposite to the outflow direction of the chips. The normal vector of the rake face can be solved using the equation of the edge line of the ball–end milling cutter and the rake angle of the ball–end milling cutter. The vector equation of the edge line of the ball–end milling cutter can be expressed as

$$\vec{r}_{ji}(\psi) = R(\psi_i) \left[ \cos \psi_{ji} \vec{i} + \sin \psi_{ji} \vec{j} \right] + \frac{R \psi_i}{\tan \beta_0} \vec{k} \tag{17}$$

In the formula,  $j$  represents the  $j$ -th tooth of the tool,  $i$  represents any cutting element on the current tooth,  $\beta_0$  is the helix angle,  $\psi_i$  is the helix lag angle,  $\psi_{ji}$  is the lag angle of the  $j$ -th tooth at this position,  $R(\psi_i)$  is the radius of the circular section under  $\psi_i$ , and the vector equation  $\vec{r}_{ji}(\psi)$  is the expression in the tool coordinate system.  $\vec{i}$ ,  $\vec{j}$  and  $\vec{k}$  are the unit vectors of each axial direction in the tool coordinate system. The angle and force analysis of the ball–end milling cutter is shown in Figure 13 below.

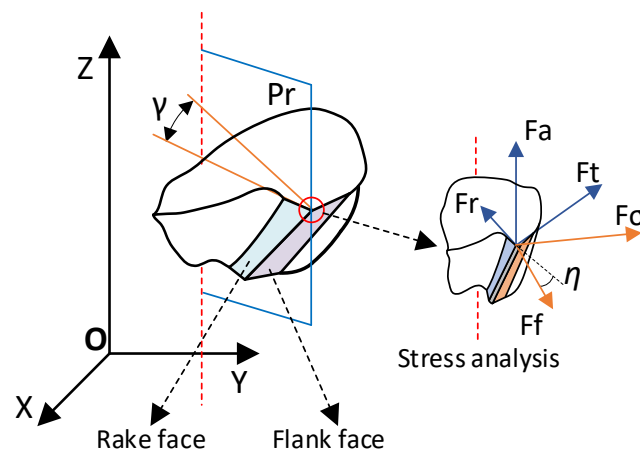


Figure 13. Ball–end milling cutter milling force analysis.

In Figure 13,  $\gamma$  is the rake angle of the ball-end milling cutter,  $\eta$  is the chip flow angle, and  $Pr$  is the base plane of the datum reference plane. Assuming that the coordinate of a certain cutting micro-element is  $(x_0, y_0, z_0)$ , the relationship between the  $Fr, Ft, Fa$  milling force coordinate system of the micro-element point and the tool coordinate system is the space translation amount  $T$  and angle of rotation around the  $Z$  axis  $a$ . (where  $T = \sqrt{(x_0^2 + y_0^2 + z_0^2)}$ ,  $\alpha = 180 + \psi_{ji}$ ). In the  $r, t, a$  force system coordinate, the normal vector  $\vec{R}_{jl2}$  of the rake face in the coordinate can be obtained through the rake angle  $\gamma$ . The edge line equation  $\vec{r}_{jl2}(\psi)$  of the ball-end milling cutter at this point can be converted into  $\vec{R}_{jl1}$  in the force system coordinate. Then, the normal vector of the rake face can be expressed as

$$\vec{n}_{jl} = f\left(\vec{R}_{jl1}, \vec{R}_{jl2}\right) \quad (18)$$

In the formula,  $\vec{n}_{jl}$  is the normal vector of the rake face, which has a vertical relationship with  $\vec{R}_{jl1}, \vec{R}_{jl2}$ .

The direction vector of the rake face friction force is in the rake face and is opposite to the direction of the cutting flow angle  $\eta$ . Therefore, the friction direction vector can be expressed as

$$\vec{n}_{fl} = g\left(\vec{R}_{jl2}, \vec{n}_{jl}, \eta\right) \quad (19)$$

By decomposing the positive pressure and friction of the rake face into the directions of  $r, t, a$  and then accumulating, the component forces of the force on the rake face in the radial, tangential, and axial directions can be solved:

$$\begin{aligned} F_{r2} &= \frac{1}{N} \sum_{k=1}^N \left( F_{\sigma g2k} * \frac{\vec{n}_{jl}}{|\vec{n}_{jl}|} \cdot \vec{r} + F_{fg2k} * \frac{\vec{n}_{fjl}}{|\vec{n}_{fjl}|} \cdot \vec{r} \right) \\ F_{t2} &= \frac{1}{N} \sum_{k=1}^N \left( F_{\sigma g2k} * \frac{\vec{n}_{jl}}{|\vec{n}_{jl}|} \cdot \vec{t} + F_{fg2k} * \frac{\vec{n}_{fjl}}{|\vec{n}_{fjl}|} \cdot \vec{t} \right) \\ F_{a2} &= \frac{1}{N} \sum_{k=1}^N \left( F_{\sigma g2k} * \frac{\vec{n}_{jl}}{|\vec{n}_{jl}|} \cdot \vec{a} + F_{fg2k} * \frac{\vec{n}_{fjl}}{|\vec{n}_{fjl}|} \cdot \vec{a} \right) \end{aligned} \quad (20)$$

In the formula,  $\vec{r}, \vec{t}$ , and  $\vec{a}$  are the axial unit vectors of the force system coordinate.  $\vec{n}_{jl}$  is the normal vector of the rake face of the  $k$ -th element of the rake face, and  $\vec{n}_{fjl}$  is the direction vector of the friction force.

At this time, the milling force of the ball-end milling cutter for processing thin-walled parts is

$$\begin{aligned} F_r &= F_{r1} + F_{r2} \\ F_t &= F_{t1} + F_{t2} \\ F_a &= F_{a1} + F_{a2} \end{aligned} \quad (21)$$

where  $F_r, F_t$  and  $F_a$  refer to the radial, tangential, and axial components of the milling force;  $F_{r1}, F_{t1}$  and  $F_{a1}$  refers to the component of milling force experienced by the cutting edge.;  $F_{r2}, F_{t2}$  and  $F_{a2}$  are the component of milling force received by the front face;

#### 4. Digital-Twin Model Optimization Module

##### 4.1. Parameter Optimization Evaluation Rules

A reasonable selection of milling parameters is the key to ensuring machining cost, machining quality, tool life, and machining efficiency. The optimization of impeller blade milling should ensure machining accuracy, minimize surface machining errors, and improve machining efficiency. This article selects machining error,  $e$ , and machining efficiency,

$MRR$  as the optimization objectives. The optimized parameters are rotational speed,  $v$ ; feed per tooth  $fz$ ; the axial depth of the cut,  $ap$ ; and the radial depth of the cut,  $ae$ .

The relationship between optimization parameters and optimization objectives, as well as the establishment of evaluation rules for optimization effects, should be established before processing parameter optimization and after the specific processing object and process are clearly determined. Parameters such as rotational speed,  $v$ ; feed rate per tooth,  $fz$ ; axial cutting depth,  $ap$ ; and radial cutting depth,  $ae$  are input into the evolutionary knowledge base established in this article to obtain machining errors and the machining efficiency of this process. Due to the fact that both cannot achieve optimal results at the same time during optimization, the evaluation function is constructed by weighting both. The model is as follows:

$$S = a * e + b * MMR \quad (22)$$

In the formula,  $S$  is evaluation;  $e$  and  $MMR$  are processing error and processing efficiency, respectively;  $S_{table}$  is processing stability threshold. The block diagram of the algorithm is shown in Figure 14.

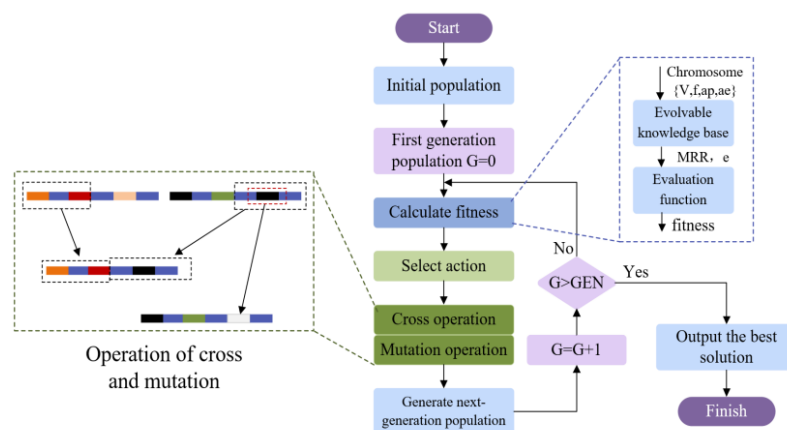


Figure 14. Genetic algorithm framework of digital-twin.

The principle of the optimization process of a genetic algorithm is to simulate the survival of the fittest in nature. The core process of the algorithm can be roughly divided into five processes: 1. Generate ethnic groups; 2. Eliminate ethnic groups based on fitness; 3. Generate new ethnic groups; 4. Eliminate groups again; 5. Repeat 3–4 times until the result meets the requirements. The specific process is shown in Figure 14. The right side of the figure shows the process of population crossing and variation. In the fitness calculation section, the fitness of each chromosome can be obtained through the digital-twin evolvable knowledge base and the evaluation function constructed in this chapter.

## 4.2. Digital-Twin Model Test Verification and Analysis

### 4.2.1. Digital-Twin Model Control Test

The experimental machine tool is an open five-axis vertical CNC milling machining center. The machine tool adopts a spindle workbench rotation structure. The technical parameters of the equipment are as Table 2:

**Table 2.** Technical parameters of vertical five-axis CNC milling center.

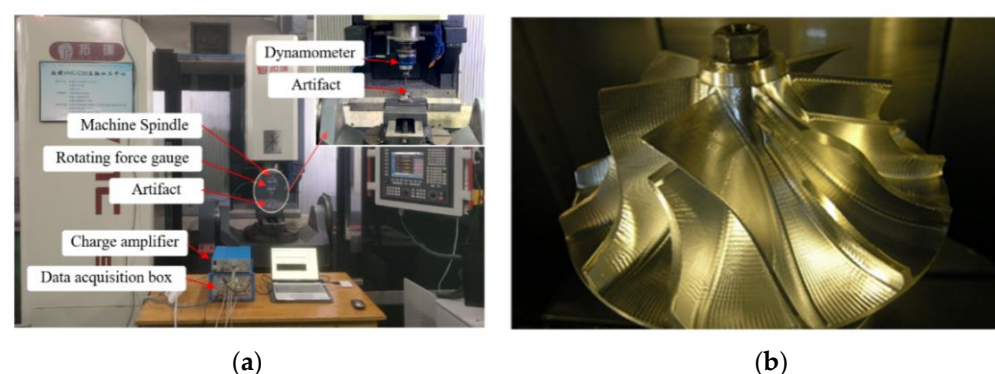
Parameter	Numerical Value	Parameter	Numerical Values
Speed rad/min	15,000	The $x$ -axis is the travel of the table/mm	1050
Spindle power/KW	11	The $y$ -axis is the travel of the table/mm	560
Maximum feed speed 25 m/min	2600	The $z$ -axis is the travel of the table/mm	450
Positioning accuracy/mm	0.005	The $a$ -axis is the travel of the table/ $^{\circ}$	$-25^{\circ}/100^{\circ}$
Cooling method	Oil cooled	The $c$ -axis is the travel of the table/ $^{\circ}$	$N*360^{\circ}$

The parameters of the processed impeller are shown in the following Table 3:

**Table 3.** Parameters of processed impeller.

Parameter	Numerical Value	Parameter	Numerical Values
Speed rad/min	15,000	The $x$ -axis is the travel of the table	1050 mm
Spindle power(KW)	11	The $y$ -axis is the travel of the table	560
Maximum feed speed 25 m/min	2600	The $z$ -axis is the travel of the table	450
Positioning accuracy is 0.005 mm	$4^{\circ}$	The $a$ -axis is the travel of the table	$-25^{\circ}/100^{\circ}$
Cooling method	Oil cooled	The $c$ -axis is the travel of the table	$N*360^{\circ}$

The test procedure is the final procedure. The machining parameter before optimization is rotational speed of 8000 r/min, feed per tooth of 0.0625 mm, and a radial depth of cut and axial depth of cut of 0.3 mm and 0.1 mm, respectively. The test equipment and workpiece are shown in Figure 15.

**Figure 15.** Schematic diagram of test equipment. (a) Machine tool and test equipment; (b) workpiece.

As shown in Figure 15, a Kistler9257B dynamometer and Kistler5007 charge amplifier were used in the experiment to collect cutting force signals. At the beginning of the experiment, we made sure that the Kistler9257B dynamometer and Kistler5007 charge amplifier were connected to each other and that they were connected to a suitable power supply. Then, we configured the Kistler 5007 charge amplifier. The force sensor was mounted on a tool head fixture in an open five-axis vertical CNC milling center. The sensor was used to collect the signal of the cutter milling force when cutting the workpiece.

The comparison between the measured data in physical space and the simulated milling force data fed back from virtual space is shown in Figure 16. The entity diagram consists of two parts: 1. Measured milling force data; 2. Comparison of local milling force data with virtual space simulation data.

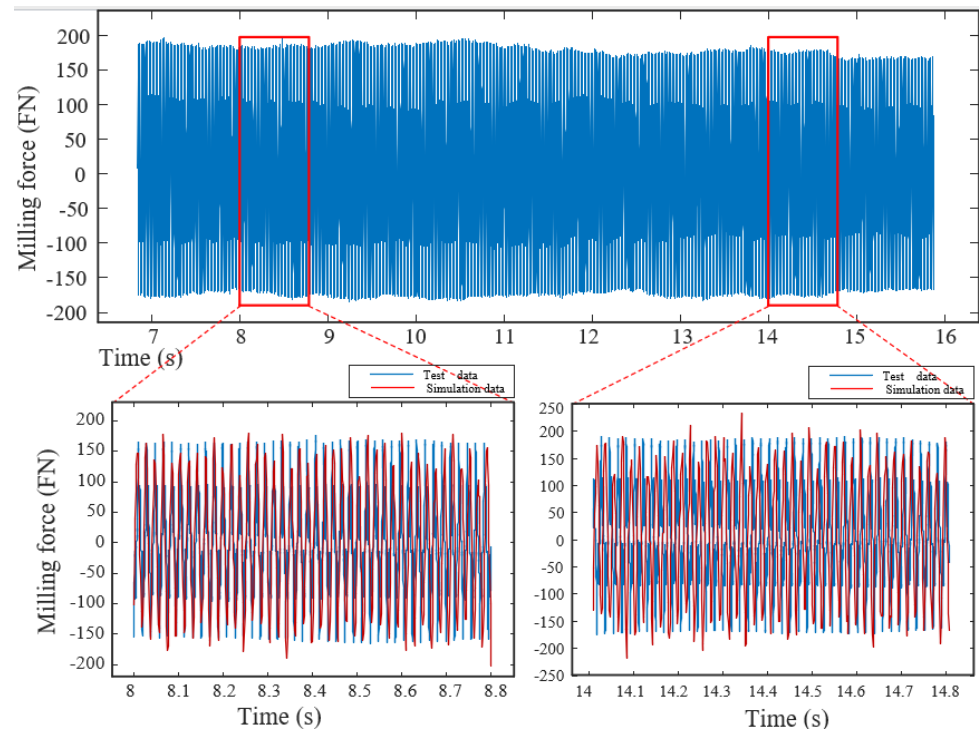


**Figure 16.** Comparison of measured data and simulation data of milling force control group.

The blue curve in Figure 16 is the measured data of milling force. The red part is virtual space milling force simulation data. The comparison error between the simulated and experimental cutting forces in the two selected areas is large. Therefore, these two parts are selected as observation data. The reason for this is that the curvature of the profile in these two areas changes dramatically, which leads to the drastic change in milling force. In the comparison of the two, the simulation data quality is good, but there are some fluctuations. The reason for this is that milling force calculation in virtual space is derived from solving the cutting contact area and milling force of the ball-end milling cutter. The chip contact area is solved via finite element simulation. The simulation model can reach the optimal solution after several rounds of debugging. The simulation model has some error fluctuation before reaching the optimal solution.

The sampling frequency of the measured data is 8000 HZ, and the selection time for the comparison part is about 0.8 s. In the two comparative figures, the ball-end milling cutter experiences a total of 21 rotation cycles. The simulation data correspond to this. The prediction error between the measured data and simulation data is calculated. Data peaks and amplitudes are selected as evaluation tools. The calculation formula is as follows:

$$P_e = \frac{1}{n} \sum_{i=1}^n \frac{P_{si} - P_{fi}}{P_{si}} \quad (23)$$

$$A_e = \frac{1}{n} \sum_{i=1}^n \frac{A_{si} - A_{fi}}{A_{si}} \quad (24)$$

In the formula,  $P_{si}$  and  $P_{fi}$  are the measured data peak value and the simulated data peak value of the  $i$ -th cycle, respectively;  $n$  is the number of cycles,  $i = 1, 2, \dots, n$ ;  $P_e$  is the

peak prediction error.  $A_{si}$  and  $A_{fi}$  are the measured data amplitude and the simulated data amplitude of the  $i$ -th cycle, respectively;  $A_e$  is the amplitude prediction error.

Using Formulas (23) and (24) to calculate 90 sets of data, the peak prediction error and amplitude prediction error of part 1 in the control group data are 7.34% and 5.57%, respectively. The peak prediction error and amplitude prediction error of local 2 are 8.21% and 6.65%, respectively. The maximum values of peak prediction error and amplitude prediction error for each cycle of local 1 are 13.21% and 14.69%, respectively. The peak prediction error and amplitude prediction error of local 2 are 18.62% and 18.32%, respectively. In the control group, the maximum error between the peak prediction error and amplitude prediction error does not exceed 8.21%. This indicates that the milling force simulation data of the virtual entity is already relatively close to the measured data in terms of overall accuracy. The maximum peak prediction error can reach 18.62%. The peak prediction error and amplitude prediction error in tool milling workpiece are mainly caused by the comprehensive influence of factors such as the complexity of cutting process, variability in material properties, changes in cutting parameters, tool wear and breakage, cutting fluid and lubrication conditions, and measurement error and sensor restrictions. This indicates that the mapping of virtual space still needs to be optimized in terms of details. In the control group, the virtual space optimization module needs to be validated. The evolutionary knowledge base module can also increase the mapping accuracy of virtual space by fine-tuning based on feedback.

#### 4.2.2. Experiments of the Digital-Twin Model Experimental Group

After the completion of the control group in the digital-twin model, the optimization module obtains the optimized processing parameters for this process in the virtual space. The specific values are a rotational speed of 9200 r/min, and feed rate per tooth of 0.0313 mm, and the radial cutting depth and axial cutting depth are 0.25 mm and 0.20 mm. We set the processing parameters of this group as the experimental group and conduct experiments. Figure 17 shows the comparison between the measured data collected by the physical space sensor and the simulated milling force fed back by the virtual space during the test.

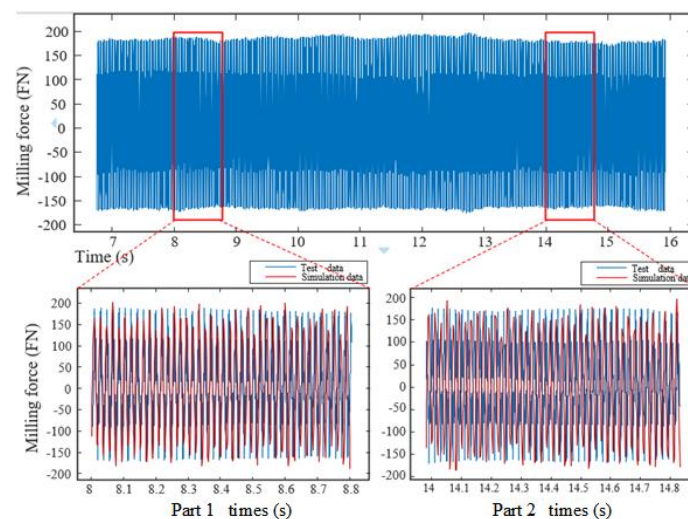


**Figure 17.** Comparison between measured data and simulation data of milling force in the experimental group.

Table 4 shows the comparison of prediction errors between the control group and the experimental group. In the experimental group, the peak prediction error and amplitude prediction error in part 1 are 7.39% and 5.59%, respectively. The peak prediction error and amplitude prediction error in part 2 are 7.9% and 6.75%, respectively. The maximum peak prediction error and amplitude prediction error for each period in part 1 are 11.5% and

11.48%, respectively. The maximum peak prediction error values for each period in part 2 are 12.5% and 13.77%, respectively.

**Table 4.** Comparison of prediction errors between the control group and the experimental group.

Data/Prediction Error	Peak Error	Amplitude Error	Maximum Peak Error	Maximum Amplitude Error
Control group 1	7.34%	5.57%	13.21%	14.69%
Test group 1	7.39%	5.59%	11.5%	11.48%
Control group 2	8.21%	6.65%	18.62%	18.32%
Test group 2	7.9%	6.75%	12.5%	13.77%

As shown in Table 4, the peak error and amplitude error of the experimental group remain stable. The maximum value of the peak error and the maximum value of the amplitude error shows an obvious downward trend. In local 2, the maximum value of peak prediction error decreases by 32.82%, and the maximum value of amplitude prediction error decreases by 24.84%. At the same time, the experimental data also show that the adjustment of the evolutionable knowledge base module obviously improves the mapping accuracy of virtual space.

#### 4.2.3. Discussion on Measurement Data of Impeller Blade Profile Error

In order to verify the accuracy of the dynamic error optimization method of impeller blade machining which is based on digital–twin technology, it is necessary to compare and judge the surface quality of the impeller blade after machining. Therefore, a three–coordinate measuring machine was used to detect the contour error of the blade before and after milling optimization. The coordinate measuring model number is Hexagon PMM–700 (Hexagon, Stockholm, Sweden). The measurement site is shown in Figure 18.

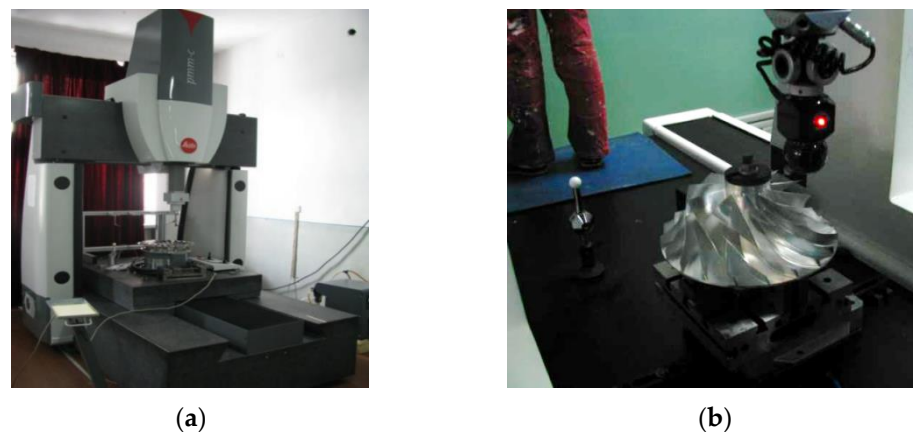


**Figure 18.** Measuring instrument and measuring scene. (a) Hexagon PMM–700; (b) actual measurement scene.

The specific measurement process is shown in Figure 19. Firstly, 16 optimal spatial position points (red) were selected on the measured blade. Secondly, the impeller was fixed on the measuring platform of the CMM. Finally, the blade was measured according to the measurement process. The test data are shown in Tables 5 and 6.

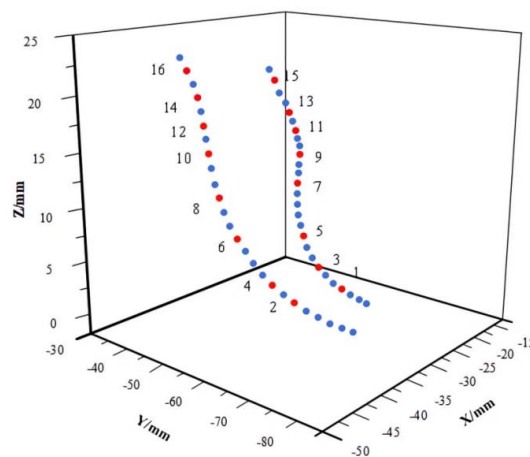


Figure 19. Blade profile error detection point.

Table 5. Control group workpiece contour deviation detection data.

Name	Deviation	Refer-X	Refer-Y	Refer-Z	Measure-X	Measure-Y	Measure-Z
C001	0.1908	-35.4959	-70.5772	13.6864	-35.9428	-70.7604	13.6535
C002	0.1969	-35.7894	-70.8760	16.0371	-35.1890	-70.0496	16.0055
C003	0.3427	-36.0747	-60.2227	19.1029	-36.4087	-60.2957	19.0782
C004	0.1952	-36.5743	-58.5549	20.3823	-36.7770	-58.5856	20.3726
C005	0.2189	-38.2148	-55.5444	22.1072	-38.4213	-58.5526	22.0261
C006	0.2315	-38.7591	-52.4318	24.9614	-38.9826	-52.4152	24.9032
C007	0.1708	-42.3633	-48.6112	26.6700	-43.0371	-48.5946	26.5191
C008	0.1791	-43.8166	-44.9163	29.2822	-43.0138	-29.8878	29.1482
C009	0.1518	-43.3029	-43.4705	33.5623	-43.5723	-43.4053	33.4193
C010	0.2407	-43.0976	-42.1685	36.0519	-42.9160	-42.1691	36.2098
C011	0.1947	-42.5740	-46.7001	37.0076	-42.3747	-47.0267	37.1289
C012	0.2450	-42.5818	-47.1489	39.1056	-41.9664	-47.1790	38.9184
C013	0.2774	-37.1423	-47.9029	40.5872	-37.8828	-49.1982	39.6851
C014	0.2644	-37.6970	-49.6733	41.5810	-37.4448	-50.1837	40.4595
C015	0.1751	-36.7832	-59.4247	43.3747	-36.8333	-59.4769	43.2344
C016	0.2649	-35.0406	-58.1229	42.6113	-36.7836	-58.0864	43.6643

Table 6. Test data of workpiece contour deviation in experimental group.

Name	Deviation	Refer-X	Refer-Y	Refer-Z	Measure-X	Measure-Y	Measure-Z
C001	0.1608	-35.3359	-70.5001	13.1862	-35.8664	-71.2604	14.0235
C002	0.1669	-35.1653	-70.1356	16.0355	-35.2210	-70.0096	15.8051
C003	0.1927	-37.3454	-61.2227	19.2588	-37.4022	-61.0021	19.556
C004	0.1852	-36.1733	-58.1519	19.8823	-36.5710	-58.2853	19.0211
C005	0.1789	-39.2036	-54.3177	21.9072	-39.5656	-54.4426	21.8856
C006	0.1415	-41.5497	-51.9996	24.3301	-41.8897	-51.7325	24.8688
C007	0.1708	-43.4464	-49.5998	27.3200	-43.0358	-48.9940	27.5111
C008	0.1791	-44.0243	-49.7780	30.1663	-44.0212	-49.8848	30.1168
C009	0.1518	-45.0251	-43.8805	34.4544	-45.4432	-44.0021	34.0023
C010	0.2207	-46.0877	-42.1511	35.8522	-42.889	-43.0501	36.1231
C011	0.1947	-44.4610	-47.1134	38.0016	-42.5445	-47.5017	37.5551
C012	0.1850	-43.1838	-48.0211	38.7056	-41.7711	-48.1121	38.3211
C013	0.1774	-38.0198	-47.8990	40.5587	-38.9886	-49.9969	39.5616
C014	0.1644	-38.9989	-48.0532	41.0023	-38.0112	-50.6689	40.5588
C015	0.1842	-37.7842	-47.1042	41.1024	-37.7632	-48.5631	40.9451
C016	0.1949	-36.0902	-59.4229	43.3356	-36.8898	-59.0565	43.7441

During the experiment, 16 points on the blade profile were selected for contour error detection. The error detection data for the control group and the experimental group are shown below.

The workpiece contour deviation detection data before and after optimization were visualized. The machined surface quality and contour deviation data of blades in the control group and the experimental group are shown in Figures 20 and 21.

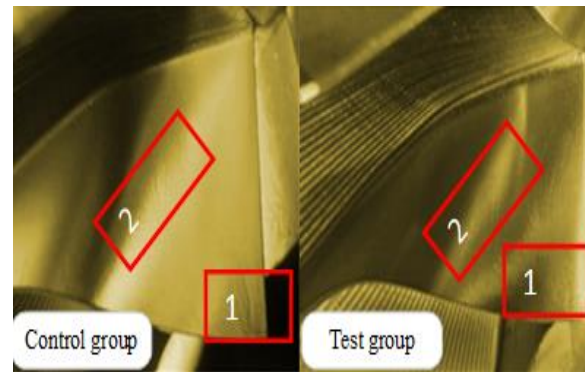


Figure 20. Surface quality optimization results.

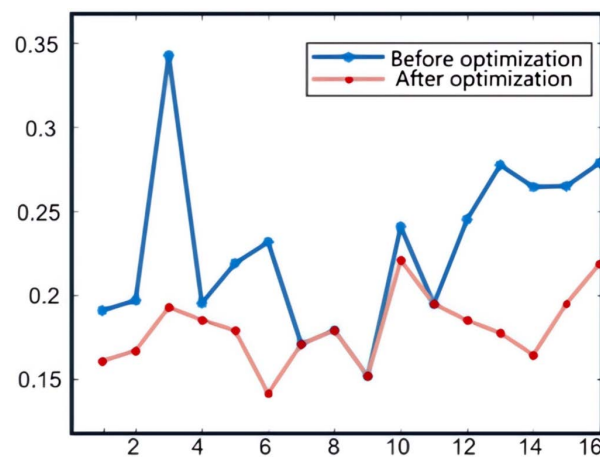


Figure 21. Optimize the results of front and rear contour error detection.

Regions 1 and 2 marked in Figure 20 are the two regions where the curvature of the impeller blade has undergone serious changes. The corresponding point of region 1 is C003, and that of region 2 is C010. The data solution results in Tables 5 and 6 show that the parameters optimized for machining errors effectively improve the workpiece surface quality. It can be seen from Figures 20 and 21 that the maximum deviation of blade machining profile error before machining error optimization is 0.3486 mm, and the overall contour error curve slope is steeper and meaner. After machining error evaluation optimization, the maximum deviation of blade contour error is 0.2298 mm, and the slope of the overall contour error curve is more gentle. According to the contour deviation data in Tables 5 and 6, the mean value of blade contour error detected after machining error optimization decreases by 20.86%. The peak profile error is reduced by 35.6%. It can be seen that the dynamic error optimization method of impeller blade machining based on digital–twin technology proposed in this paper can effectively improve the workpiece surface quality.

## 5. Conclusions

In this paper, a method of machining error prediction and intelligent control considering the time–varying effect of tool wear is proposed based on digital–twin technology. This

method combines machine tool information and the machining position during the machining process with the iterative prediction model of milling force to achieve the prediction of machining errors under the dynamic load of TC4 impeller blades. The experiment shows that in terms of dynamic milling force prediction, the average error after optimization does not exceed 8%. The maximum error shall not exceed 14%. In terms of processing the error control effect, the average contour error of the optimized workpiece decreases by about 20%. The peak contour error decreases by about 35%. The main contributions in this field of work are as follows:

1. A digital–twin model based on the complex process of impeller blades was proposed. This model achieves the iterative feedback optimization of machining parameters for impeller blades. A TC4 digital–twin model has been established for specific machining process levels, achieving the data optimization of complex machining processes for impeller blades.
2. Based on the digital–twin model, this article constructs an evolutionary knowledge base for impeller blade machining. Through secondary development, point cloud data are extracted from ABAQUS to construct a knowledge base, accurately expressing the contact relationship between tools and workpieces. At the same time, the tool wear model is established in the evolutionary knowledge base. The evolutionary knowledge base takes the spatial position information of the machine tool spindle and the angles of the turntable and swing table as real–time inputs. Based on rolling data and tool wear model, a milling force prediction model under the condition of tool wear was constructed. The prediction error of this model is less than 20%.
3. Based on the coupling relationship between milling force and machining error, this article establishes an iterative model for milling force and machining error. This model achieves real–time feedback process control through data rolling and process iteration optimization based on machining quality evaluation. The digital–twin system calculates through an embedded model that the average time it takes to send out active control signals is less than 500 milliseconds. This improves the mapping accuracy of the digital–twin model.

This study has implemented the application of digital–twinning in the optimization of machining errors in weakly rigid thin–walled parts. However, there are still limitations in this study. They mainly include the influence of external factors when establishing the tool wear model and the continuous evolution of the optimization model driven by sensor data. In this study, dynamic machining error prediction and intelligent control were achieved by combining the digital–twin model of the machining process with a multi–objective machining algorithm. Other processing factors such as the surface roughness of the tool workpiece and tool life were not taken into account. In the future, the real–time perception of the entire process of CNC machining based on multi–sensor fusion technology will be an important research direction. In order to improve the accuracy of machining parameter optimization and achieve better machining performance, it is necessary to conduct dynamic evolution research on the model driven by data fusion and intelligent algorithms.

**Author Contributions:** Conceptualization, S.W. (Shanchao Wang) and R.L.; methodology, S.W. (Shanchao Wang), R.L. and X.L.; software, S.W. (Shanchao Wang); validation, C.W., X.Z. and S.W. (Shanshan Wang); formal analysis, R.L. and B.Z.; investigation, R.L.; resources, X.L. and R.L.; writing—original draft preparation, S.W. (Shanshan Wang); writing—review and editing, S.W. (Shanshan Wang) and R.L.; funding acquisition, X.L. and R.L. All authors have read and agreed to the published version of the manuscript.

**Funding:** The authors are grateful for financial support from the Natural Science Foundation of Heilongjiang Province (No. TD2022E003), the Open Fund of Key Laboratory of Advanced Manufacturing and Intelligent Technology, Ministry of Education (No. KFKT202202), the Heilongjiang Provincial Department of Education Young Innovative Talents Training Program for General Undergraduate Higher Education Institutions (UNPYSCT-2020196), and the General program of National Natural Science Foundation of China (52075135).

**Institutional Review Board Statement:** Not applicable.

**Informed Consent Statement:** Not applicable.

**Data Availability Statement:** Not applicable.

**Conflicts of Interest:** The authors declare no conflict of interest.

## References

1. Rosen, R.; Von Wichert, G.; Lo, G.; Bettenhausen, K.D. About The Importance of Autonomy and digital-twins for the Future of Manufacturing. *IFAC-Pap.* **2015**, *48*, 567–572. [[CrossRef](#)]
2. Grieves, M.W. Product Lifecycle Management: The New Paradigm for Enterprises. *Int. J. Prod. Dev.* **2005**, *2*, 71. [[CrossRef](#)]
3. Fei, T.; Liu, W.; Liu, J.; Liu, X. Digital-twin and Its Potential Application Exploration. *Comput. Integr. Manuf. Syst.* **2018**, *24*, 1–18. [[CrossRef](#)]
4. Fei, T.; Liu, W. Five-dimension digital-twin Model and Its Ten Applications. *Jisuanji Jicheng Zhizao Xitong/Comput. Integr. Manuf. Syst.* **2019**, *25*, 1–18.
5. Liu, J.; Zhao, P.; Jing, X.; Cao, X.; Sheng, S.; Zhou, H.; Liu, X.; Feng, F. Dynamic design method of digital-twin process model driven by knowledge-evolution machining features. *Int. J. Prod. Res.* **2021**, *60*, 2312–2330. [[CrossRef](#)]
6. Hänel, A.; Seidel, A.; Frieß, U.; Teicher, U.; Wiemer, H.; Wang, D.; Wenkler, E.; Penter, L.; Hellmich, A.; Ihlenfeldt, S. Digital-twins for High-Tech Machining Applications—A Model-Based Analytics-Ready Approach. *J. Manuf. Mater. Process.* **2021**, *5*, 80. [[CrossRef](#)]
7. Bao, J.; Guo, D.; Li, J.; Zhang, J. The Modelling and Operations for The Digital-twin in the Context of Manufacturing. *Enterp. Inf. Syst.* **2019**, *13*, 534–556. [[CrossRef](#)]
8. Delbrügger, T.; Rossmann, J. Representing Adaptation Options in Experimentable Digital-Twins of Production Systems. *Int. J. Comput. Integr. Manuf.* **2019**, *32*, 352–365. [[CrossRef](#)]
9. Luo, W.; Hu, T.; Zhang, C.; Wei, Y. digital-twin for CNC machine tool: Modeling and using strategy. *J. Ambient. Intell. Humaniz. Comput.* **2019**, *10*, 1129–1140. [[CrossRef](#)]
10. Xuemin, S.; Jinsong, B.; Jie, L.; Yiming, Z.; Shimin, L.; Bin, Z. A digital-twin-driven approach for the assembly-commissioning of high precision products. *Robot. Comput. Integr. Manuf.* **2020**, *61*, 101839.
11. Hänel, A.; Schnellhardt, T.; Wenkler, E.; Nestler, A.; Brosius, A.; Corinth, C.; Fay, A.; Ihlenfeldt, S. The development of a digital-twin for machining processes for the application in aerospace industry. *Procedia CIRP* **2020**, *93*, 1399–1404. [[CrossRef](#)]
12. Liu, S.; Bao, J.; Lu, Y.; Li, J.; Lu, S.; Sun, X. digital-twin modeling method based on biomimicry for machining aerospace components. *J. Manuf. Syst.* **2020**, *58*, 180–195. [[CrossRef](#)]
13. Mukherjee, T.; Debroy, T. A digital-twin for rapid qualification of 3D printed metallic components. *Appl. Mater. Today* **2018**, *14*, 59–65. [[CrossRef](#)]
14. Söderberg, R.; Wärmefjord, K.; Carlson, J.S.; Lindkvist, L. Toward a digital-twin for real-time geometry assurance in individualized production. *CIRP Ann. Manuf. Technol.* **2017**, *66*, 137–140. [[CrossRef](#)]
15. Glatt, M.; Sinnwell, C.; Yi, L.; Donohoe, S.; Ravani, B.; Jan, C. Aurich. Modeling and Implementation of A Digital-Twin of Material Flows Based on Physics Simulation. *J. Manuf. Syst.* **2021**, *15*, 231–245. [[CrossRef](#)]
16. Zhao, L.; Fang, Y.; Lou, P.; Yan, J. Cutting Parameter Optimization for Reducing Carbon Emissions Using digital-twin. *Int. J. Precis. Eng. Manuf.* **2021**, *22*, 933–949. [[CrossRef](#)]
17. Ratchev, S.; Liu, S.; Becker, A.A. Error compensation strategy in milling flexible thin-wall parts. *J. Mater. Process. Technol.* **2005**, *162*, 673–681. [[CrossRef](#)]
18. Chen, W.; Xue, J.; Tang, D.; Chen, H.; Qu, S. Deformation prediction and error compensation in multilayer milling processes for thin-walled parts. *Int. J. Mach. Tools Manuf.* **2009**, *49*, 859–864. [[CrossRef](#)]
19. Wang, L.; Si, H. Machining deformation prediction of thin-walled workpieces in five-axis flank milling. *Int. J. Adv. Manuf. Technol.* **2018**, *97*, 4179–4193. [[CrossRef](#)]
20. Liu, C.; Li, Y.; Shen, W. A real time machining error compensation method based on dynamic features for cutting force induced elastic deformation in flank milling. *Mach. Sci. Technol.* **2018**, *22*, 766–786. [[CrossRef](#)]
21. Yue, C.; Chen, Z.; Liang, S.Y.; Gao, H. Modeling machining errors for thin-walled parts according to chip thickness. *Int. J. Adv. Manuf. Technol.* **2019**, *10*, 91–100. [[CrossRef](#)]
22. Chen, Z.; Yue, C.; Liang, S.Y.; Liu, X.; Li, H. Iterative from error prediction for side-milling of thin-walled parts. *Int. J. Adv. Manuf. Technol.* **2020**, *107*, 4173–4189. [[CrossRef](#)]
23. Archard, F. Contact and Rubbing of Flat Surfaces. *J. Appl. Phys.* **1953**, *24*, 981–988. [[CrossRef](#)]
24. Sun, Y.; Jiang, S. Predictive modeling of chatter stability considering force-induced deformation effect in milling thin-walled parts. *Int. J. Mach. Tools Manuf.* **2018**, *135*, 38–52. [[CrossRef](#)]
25. Sun, Y.; Jia, J.; Xu, J.; Chen, M.; Niu, J. Path Feedrate and Trajectory Planning for Free-Form Surface Machining: A State-of-the-Art Review. *Chin. J. Aeronaut.* **2022**, *35*, 12–29. [[CrossRef](#)]
26. Sun, Y.; Zheng, M.; Jiang, S.; Zhan, D.; Wang, R. A State-of-the-Art Review on Chatter Stability in Machining Thin-Walled Parts. *Machines* **2023**, *11*, 359. [[CrossRef](#)]

27. Liu, X.; Li, R.; Wu, S.; Yang, L.; Yue, C. A prediction method of milling chatter stability for complex surface mold. *Int. J. Adv. Manuf. Technol.* **2017**, *89*, 2637–2648. [[CrossRef](#)]
28. Pirso, J.; Letunovit, S.; Viljus, M. Friction and wear behaviour of cemented carbides. *Wear* **2004**, *257*, 257–265. [[CrossRef](#)]
29. Lancaster, J.K. The influence of substrate hardness on the formation and endurance of molybdenum disulphide films. *Wear* **1965**, *10*, 103–117. [[CrossRef](#)]
30. Ge, G.; Du, Z.; Yang, J. Rapid prediction and compensation method of cutting force-induced error for thin-walled workpiece. *Int. J. Adv. Manuf. Technol.* **2020**, *106*, 5453–5462. [[CrossRef](#)]
31. Lee, P.; Altinta, Y. Prediction of ball-end milling forces from orthogonal cutting data. *Int. J. Mach. Tools Manuf.* **1996**, *36*, 1059–1072. [[CrossRef](#)]
32. Gradisek, J.; Kalveram, M.; Weinert, K. Mechanistic identification of specific force coefficients for a general end mill. *Int. J. Mach. Tools Manuf.* **2004**, *44*, 401–414. [[CrossRef](#)]
33. Budak, E.; Ozlu, E. Development of a thermomechanical cutting process model for machining process simulations. *CIRP Ann. Manuf. Technol.* **2008**, *57*, 97–100. [[CrossRef](#)]
34. Özlü, E.; Budak, E.; Molinari, A. Thermomechanical modeling of orthogonal cutting including the effect of stick-slide regions on the rake face. In Proceedings of the 10th CIRP International Workshop on Modeling of Machining Operations, Reggio Calabria, Italy, 27–28 August 2007; University of Calabria: Arcavacata, Italy, 2007.

**Disclaimer/Publisher’s Note:** The statements, opinions and data contained in all publications are solely those of the individual author(s) and contributor(s) and not of MDPI and/or the editor(s). MDPI and/or the editor(s) disclaim responsibility for any injury to people or property resulting from any ideas, methods, instructions or products referred to in the content.